New UV-Curable Anticorrosion Coatings from Vegetable Oils

Macromolecular Materials and Engineering
www.mme-journal.de

New UV-Curable Anticorrosion Coatings from Vegetable Oils

Camilla Noè, Leonardo Iannucci, Samuel Malburet, Alain Graillot, Marco Sangermano, and Sabrina Grassini*

Bio-based epoxy resins are attracting widespread interest in the field of polymer thermosets as environmentally friendly building block. In the present study, the feasibility of applying UV-curable epoxidized vegetable oils (EVOs) as anti-corrosion coating is investigated. Rheological characterization of EVOs is carried out, and their viscosity-shear relationship is evaluated. The cationic UV-curing of EVOs successfully gives rise to crosslinked materials with a wide range of thermo-mechanical properties, evaluated by differential scanning calorimetric analysis and dynamic thermal mechanical analysis. A high epoxy-group conversion, ranging from 93% to 99%, is always obtained. The thermal stability and surface properties of the bio-based coatings, such as, pencil hardness, adhesion, solvent resistance, and contact angle, are analyzed. Moreover, the corrosion protection effectiveness of the coatings is characterized by potentiodynamic polarization and electrochemical impedance spectroscopy measurements. In addition, field emission scanning electron microscopy is used to assess the samples morphology after corrosion tests.

1. Introduction

In the last 20 years, due to the increasing concern on the environmental pollution and fossil fuel depletion, great attention has been given to the development of new polymers from renewable resources. In fact, by using bio-based materials, the carbon dioxide emission and the non-renewable energy consumption can be reduced. However, while the availability of bio-based thermoplastic is quite large, the bio-based thermosetting field is still limited; thus, it represents a real challenge for both academics and industry.

C. Noè, Dr. L. Iannucci, M. Sangermano, S. Grassini
Politecnico di Torino
Dipartimento di Scienza Applicata e Tecnologia
C.so Duca degli Abruzzi 24, Torino 10129, Italy
E-mail: leonardo.iannucci@polito.it

S. Malburet, A. Graillot
Specific Polymers
150 Avenue des Cocardières, Castries 34160, France

The ORCID identification number(s) for the author(s) of this article can be found under https://doi.org/10.1002/mame.202100029.

DOI: 10.1002/mame.202100029

The majority of petroleum-derived thermosetting polymers are based on epoxy resins and it is also important to stress that more than 60% of the global epoxy resin production is used in coating industry.[1]

Epoxy coatings have been widely used as physical barrier to protect metals against corrosion since they possess good chemical resistance, strong adhesion, and good processability. However, their applicability is still limited since they usually absorb water due to their hydrophilic nature. The water uptake may start the metal corrosion and cause the coating delamination.[2] Therefore, many attempts have been made to reduce the surface hydrophilicity like increasing the surface roughness, introducing low surface energy materials such as fluorine or silicon containing polymers[3,4] or adding small fillers like graphene or α-alumina.[5,6] However, those coatings were obtained from petroleum-based resins. Interesting results were recently found in the characterization of bio-based epoxy coatings,[7] but in this case the protective performances were enhanced by the addition of super-hydrophobic nanoparticles.

The most used epoxy resin is the diGlycidyl ether of bisphenol-A (DGEBA), which is obtained by glycidylation of bisphenol A (BPA) with epichlorohydrin. Nevertheless, BPA is a reprotoxic substance which can induce serious damage in human endocrine system and has a negative impact on wildlife.[8] Bio-based epoxy resins are potentially able to substitute BPA.

In particular, different aromatic and cycloaliphatic bio-based coatings deriving from lignin,[9] cinnamic acid,[10] eugenol,[11] and vanillin[12–14] were developed with enhanced properties.

Moreover, new strategies to obtain sustainable competitive anticorrosion coatings have been proposed. In particular, blending petroleum-based resin with bio-based resin having flexible hydrophobic groups showed promising results.[15]

In the field of polymer coatings, the UV-curing technology is an environmentally friendly polymerization technique which can be run in absence of solvent (therefore with a very low VOC emission) and can take place at ambient temperature in a very short time. The photopolymerization reaction proceeds by a chain-growth mechanism which involves the propagation of either a radical or a cation. Cationic photocuring presents many

advantages over the widely used radical one. For example, it is not inhibited by oxygen and the reaction can continue in the dark since the Lewis acid or protic acid species generated by the photoinitiator are long-lived.[16]

By searching into the currently available scientific literature on bio-based epoxidized thermosets it can be clearly seen that the majority of the papers concern thermal curing process,[17–19] while the cation photocuring is still largely unexplored.

Crivello et al. first reported the use of cationic photocuring of different epoxidized triglycerides[20] and of pinene and limonene epoxy derivatives.[21] More recently, the reactivity toward cationic photopolymerization of cardanols derivatives was assessed in order to produce coatings.[22–24] Epoxy thermosets with promising thermo-mechanical properties were also obtained from the photocuring of furan, fatty acid derivatives and resorcinol.[25,26]

In a previous paper, our group investigated the cationic photocuring of vanillin, phloroglucinol, and castor oil epoxy derivatives.[27] We also investigated and compared the thermo-mechanical properties obtained from either UV or hardener-free thermal curing of different epoxidized vegetable oils (EVOs).[28]

To the best authors' knowledge, previous work on cationic photocuring of bio-based thermosets has focused only on the curing kinetics and on the thermo-mechanical properties of the obtained networks. So, there remains a need for assessing the coating properties and for evaluating their exploitation in different applications.

With the aim to fill this gap, this paper provides not only a fully investigation of the bio-based thermosets obtained from three different epoxidized triglycerides but also an investigation on the coating properties and on the anticorrosion performance of the obtained fully bio-based coatings.

2. Experimental Section

2.1. Materials

The cationic photoinitiator triarylsulfonium hexafluoroantimonate salts, mixed 50 wt% in propylene carbonate were purchased from Sigma-Aldrich (Milan, Italy). The epoxidized rose hip seed oils (ERHO-4.5 and ERHO-6) and epoxidized grapeseed oil (EGRP-5) were synthetized and provided by SPECIFIC POLYMERS (Castries, France). The compositions of the starting vegetable oils are reported in the **Table 1**.

In order to characterize the anti-corrosion performance of the coatings, they were deposited on low-carbon steel coupons, namely, the Q-panel standard test substrate (purchased from Q-Lab). The chemical composition of the material is: 0.10 wt% C, 0.60 wt% Mn, 0.20 wt% Ni, 0.15 wt% Cr, and balance Fe. Before coating application, metal substrates were polished using abrasive papers until 600 grit and then rinsed in distilled water and degreased with ethanol.

Table 1. Composition of the starting vegetable oils.

Vegetable oil	ERHO-4.5	EGRP-5	ERHO-6
Saturated fatty acids [%]	17	11	5
Mono-unsaturated fatty acids [%]	20	22	16
Di-unsaturated fatty acids [%]	57	67	46
Tri-unsaturated fatty acids	5	0	36
Double bonds content (m_{eq} g^{-1})	4.85	5.51	6.43

2.2. Synthesis of Epoxidized Vegetable Oils

The ERHO-4.5, EGRP-5, and ERHO-6 were synthetized following the previously reported method.[28]

Epoxidation conditions were adjusted for each vegetable oil in order to maintain the following molar ratio conditions C = C/Acetic acid/H_2O_2 (35% w/w); 1/0.5/1.5eq with amberlite IR-120 loaded at 10 wt% with respect to (w.r.t) acetic acid and hydrogen peroxide weight. Briefly, the vegetable oil (1eq of double bonds), toluene, and the acetic acid (0.5eq w.r.t double bonds) were added to the reaction mixture. Then, after few minutes, amberlite IR-120 hydrogen form (10 wt% w.r.t acetic acid and hydrogen peroxide weight) was added and the mixture was stirred at 510 rpm at 55 °C. Once the temperature reached, hydrogen peroxide aqueous solution (35%, w/w) (1.5eq w.r.t double bonds) was added dropwise over 30 min with continuous stirring. The reaction was maintained under these conditions for 24 h before that the reaction media was washed with water, dried over Na_2SO_4, and concentrated under reduced pressure at 60 °C.

2.3. Coating Preparation

The epoxidized vegetable epoxy oils were mixed with the cationic photoinitiator: Triarylsulfonium hexafluoroantimonate salts at a content of 2 phr (per hundred resin).

The films were subsequently crosslinked by Dymax ECE 5000 Flood lamp for 15 s at a light intensity of 95 mW cm^{-2}. Transparent-cured coatings were obtained. All the polymerization reactions were performed at room temperature at constant humidity (RH = 25–30%).

2.4. Characterization

2.4.1. Viscosity Measurement

The viscosity measurements were conducted with Anton Paar MCR302 using a cone-plate geometry CP50-1 with a fixed gap of 0.05 mm. The cone geometry was: diameter ⌀ = 25 mm, and cone-angle $\alpha = 1°$. All the experiments were performed on 0.57 mL volume of oil at 20 °C. The viscosity of the samples was recorded by varying the shear rate ($\dot{\gamma}$) from the highest value ($\dot{\gamma} = 100\ s^{-1}$) to the lowest value ($\dot{\gamma} = 0.1\ s^{-1}$). In order to describe the rheological behavior of the tested oils, the power law model (two terms model, Equation (1)) and the Sisko model (three-term model, Equation (2))[29] were used:

$$\eta = K\dot{\gamma}^{n-1} \quad (1)$$

$$\eta = \eta_\infty + K\dot{\gamma}^{n-1} \quad (2)$$

where η is the viscosity, $\dot{\gamma}$ is the shear rate, K is the consistency index, n the flow behavior index, and η_∞ is the viscosity at infinite shear rate.

2.4.2. Fourier Transform Infrared Spectroscopy

The Fourier transform infrared spectroscopy (FTIR) spectra were recorded with a Nicolet iS 50 Spectrometer in transmission mode in air. The samples were prepared by coating the photocurable formulations on a silicon wafer. The average film thickness was about 20 µm. The data were collected in the wavelength range of 500–4000 cm^{-1} before and after irradiation under the static DIMAX lamp.

All measurements were obtained with a scanning rate of 1 scan per 1.2 s with a spectral resolution of 4.0 cm^{-1}. The Thermo Scientific OMNIC Specta Software was used to record and process the data. All measurements were repeated three times.

2.4.3. Gel Content

The gel content was determined on the cured films by measuring the weight loss after 24 h extraction with chloroform at room temperature, according to the standard test method ASTM D2765-84.

2.4.4. Dynamic Thermal Mechanical Analysis

Dynamic thermal-mechanical analysis was performed with a Triton Technology. Samples with dimensions 11 mm x 7 mm x 0.2 mm were tested with uniaxial stretching performed with a heating rate of 3 °C min^{-1}, frequency of 1 Hz and strain of 0.02%. The storage modulus (E') and the loss factor ($\tan\delta$) were recorded as a function of temperature. In order to estimate the apparent cross-linking density (ν_c), also known as strand density, the storage modulus values in the rubbery plateau region (E'_R) were extracted from the graph at generally 50 °C above the glass transition temperature. The Equation (3) was used to calculate the ν_c. This equation derived from the statistical theory of rubber elasticity, which however is just an approximation to model the system and therefore was used only to qualitatively compare the level of crosslinking among the obtained networks.[30,31]

$$\nu_c = \frac{E'_R}{3RT} \quad (3)$$

where ν_c is the number of moles of network chains per unit volume of the cured network, R is the gas constant, T is the absolute temperature (i.e., at T_g + 50 °C).

2.4.5. Differential Scanning Calorimetric Analysis

Differential scanning calorimetric analysis (DSC) were carried out on a Mettler Toledo DSC instrument at a heating rate of 10 °C min^{-1} using a nitrogen atmosphere. Samples (10–12 mg) were sealed in a 100 µL aluminum pan with pierced lids.

2.4.6. Thermogravimetric Analysis

Thermogravimetric analysis (TGA) was performed with a Mettler Toledo TGA/SDTA 851e in order to evaluate the thermal stability of the obtained films. Samples (10–12mg) were inserted in alumina cups and heated at 10 °C min^{-1} from 30 °C to 700 °C under N_2 flux.

2.4.7. Pencil Hardness

The pencil hardness test was performed by using pencils of different grades starting from the 6H and continuing down the scale testing with softer and softer pencils according to ASTM D 3363–74. The pencils were maintained at 45° and pushed for at least 6 mm with uniform pressure and speed onto the coating surface. The hardness of the coating was taken as that of the hardest pencil which caused a cut less than 3 mm long out of the 6 mm test push on the surface of the coating.

2.4.8. Adhesion Measurement

The coating adhesion measurement was taken according to the ASTM D3359-B. The surface of each coating was scratched both vertically and horizontally with a blade holding 6 teeth, separated from each other by 2 mm distance. A strip of adhesive tape was then applied and subsequently pulled away with a 180° angle. The percentage of squares where the coating is still intact is reported.

2.4.9. Solvent Rub Resistance Test

The coating chemical resistance was evaluated by methyl ethyl ketone double rub test according to the ASTM D5402. Double rubs were performed until the substrate was exposed, or for a maximum of 200.

2.4.10. Contact Angle

Contact angle measurements were performed with a Kruss DSA10 instrument, equipped with a video camera. Analyses were made at room temperature by means of the sessile drop technique. Six measurements were performed on each sample. The surface free energy was determined on the basis of Owens-Wendt-Rabel-Kaelble (WORK) method.[32] The measuring liquids were double distilled water (γ = 72.8 mN m^{-1}) and diiodomethane (γ = 50.8 mN m^{-1}).

2.4.11. Electrochemical Characterizations

Electrochemical measurements were used to characterize the corrosion behavior of the different coatings. All measurements,

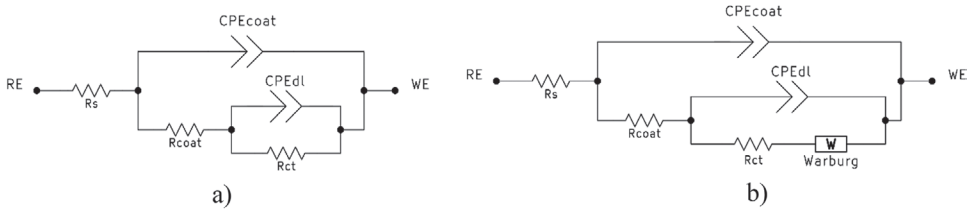

Figure 1. Electrical circuits used to model the EIS data.

performed by means of an Ivium-n-Stat potentiostat, were carried out in a 3-electrode electrochemical cell, using an Ag/AgCl electrode as the reference electrode (RE), a Ni-Cr wire as the counter electrode (CE), and the coated steel sample as the working electrode (WE), as commonly done for corrosion experiments.[33] Tests were performed in a 0.1 M NaCl (sodium chloride) aerated solution at room temperature. This solution was chosen in order to simulate a moderately aggressive environment containing chlorides, as the investigated coatings are not specifically designed for seawater applications. The exposed sample surface was 0.78 cm^2; all results here presented are scaled to the equivalent area of 1 cm^2.

Two techniques were used to investigate the corrosion protection effectiveness of the coatings: Potentiodynamic Polarization and Electrochemical Impedance Spectroscopy (EIS). Measurements were performed after monitoring the open circuit potential (OCP) of the sample for 1 h in order to reach a steady state of the system under study. Polarization curves were acquired in the range between −0.3 V versus OCP and + 2.7 V versus OCP, using a scan rate of 0.166 mV s^{-1} and a step size of 1 mV; three samples were tested for each coating formulation. Results from potentiodynamic polarization measurements were analyzed by means of Tafel extrapolation in order to characterize the corrosion kinetics. Actually, it is possible to derive the corrosion current (I_{corr}) and the corrosion potential (E_{corr}) as the intersection of the linear portions of the anodic and cathodic slopes of the polarization curve.[34] Then, it is possible to compute also the polarization resistance, using the SternGeary equation:[35]

$$R_p = \frac{1}{2.303\, I_{corr}} \left(\frac{\beta_a \times \beta_c}{\beta_a + \beta_c} \right) \tag{4}$$

where R_p is the polarization resistance, I_{corr} is the corrosion current, and β_a and β_c are the anodic and cathodic Tafel slopes, respectively. Moreover, corrosion current is an important parameter in electrochemical characterization because it allows to compute the corrosion rate:[34]

$$CR = \frac{k\, M\, I_{corr}}{\rho} \tag{5}$$

where CR is the corrosion rate (in mm per year), k is a constant equal to 3272 mm/(A cm year), M is the equivalent weight (27.92 g for iron), I_{corr} is the corrosion current (in A cm^{-2}), and ρ is the material density (7.87 g cm^{-3} for iron).

EIS measurements were performed in the frequency range between 10^{-2} and 10^4 Hz, using a signal of 10 mV and acquiring 10 points per frequency decade. Impedance spectra were acquired after 1 h of immersion in the electrolyte solution and then every 24 h for 2 weeks in order to assess the stability of the coating in contact with the aggressive solution; three samples were tested for each coating formulation. Impedance data were further analysed using equivalent electrical circuit modelling in order to derive a model for the interaction between the metal-coating system and the environment.[36] Actually, this processing enables to derive a model for the investigated physical system using conventional electrical components and thus allows to study the evolution of the different elements of the system as a function of the immersion time. Two electrical circuits have been used, which are typically employed to model coatings impedance;[37,38] they are represented in **Figure 1**.

The first one (Figure 1a) was composed by the solution resistance (R_s), the coating resistance (R_{coat}), the coating capacitance (CPE_{coat}), the resistance to charge transfer (R_{ct}), and the capacitance of the double layer (CPE_{dl}). The two capacitances had been modelled using constant phase elements (CPE) in order to take into account surface heterogeneity and thus time-constant dispersions.[39] The CPE impedance can be expressed as:

$$Z_{CPE} = \frac{1}{(j\omega)^n\, Q} \tag{6}$$

where Q is the CPE parameter having dimensions of a capacitance, $j = \sqrt{-1}$, $\omega = 2\pi f$ (f is the frequency), and n is a parameter that ranges between 0 and 1. When $n = 0$ the CPE behaves like a resistor, when $n = 1$ it behaves like a capacitor and it has an intermediate behavior in the other cases. In order to take into account the corrosion phenomena occurring on some of the samples, in these cases a second electrical circuit (see Figure 5b) was also used, where a Warburg diffusion element is positioned in series to the resistance to charge transfer. This element is related to the oxygen diffusion from the solution to the electrode surface, as oxygen is involved in the cathodic reaction occurring in the corrosion process.[37] The Warburg element can be described as a CPE in which $n = 0.5$, that is:

$$Z_W = \frac{1}{(j\omega)^{0.5}\, W} \tag{7}$$

where W is a parameter independent of frequency and has dimensions of a capacitance.[39]

Data analysis, both Tafel extrapolation and equivalent electrical circuit modelling, was performed using the software IviumSoft 4.933.

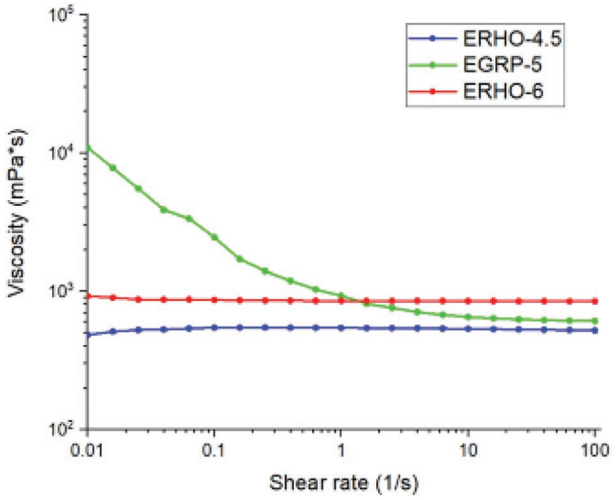

Figure 2. Viscosity of epoxidized oils as a function of shear rate at 20 °C.

2.4.12. Morphological Characterization

At the end of the 2-week immersion tests in NaCl solution, morphological characterization of the samples surface was carried out by means of electron microscopy. A field emission scanning electron microscope (FESEM Supra 40, ZEISS) was used, with an acceleration voltage of 5 kV and an aperture size of 30 µm.

3. Results and Discussion

3.1. Viscosity Evaluation

The viscosity of the photocurable resin is an important parameter to be evaluated in the coating process since their rheological behavior notably affects their performance and applicability. The epoxy oils deriving from rose hip seed oil were found to be Newtonian, showing a near constant value in the shear rate range tested. On the contrary, the epoxidized oil deriving from grapeseed oil show a shear thinning behavior since its viscosity decreases as the shear rate increases and then reaches a near-constant value (named second Newtonian region) (**Figure 2**). The rheological behaviors of ERHO-4.5 and ERHO-6 were correctly described by the power law model (Equation (1)) while the EGRP-5 fits the Sisko model (Equation (2)). The parameter values used to fit the viscosity curves were reported in the **Table 2**.

Table 2. Viscosity models parameters.

Epoxidized oil	Fitting model	K	n	η_∞ [mPa*s]	η [mPa*s]
ERHO-4.5	Power law	0.55	0.99		519
EGRP-5	Sisko	0.22	0.14	610	610[a)]
ERHO-6	Power law	0.86	1		845

[a)]value taken in the second Newtonian plateau.

The overall viscosity values obtained were higher than the ones reported with commercial vegetable oils.[29] This result can be explained considering an enhancement of the molecular weight of the oils as a consequence of the epoxidation reaction. In fact, it was previously demonstrated that in the case of saturated fatty acid esters the viscosity increases with molecular weight.[40] The obtained viscosity range is in the same order of magnitude of the one reported for epoxidized soybean oil.[41] Moreover, it is possible to observe a η enhancement with the increase of the epoxy content (ERHO-4.5 < EGRP-5 < ERHO-6) which can be due to the formation of hydrogen bonds.[42,43]

3.2. UV-Curing Process

The photocuring process was followed by measuring the epoxy group conversion upon irradiation (**Figure 3**).

The FTIR spectra of the epoxidized oils display their characteristic functional groups. The two peaks at 2926 cm^{-1} and

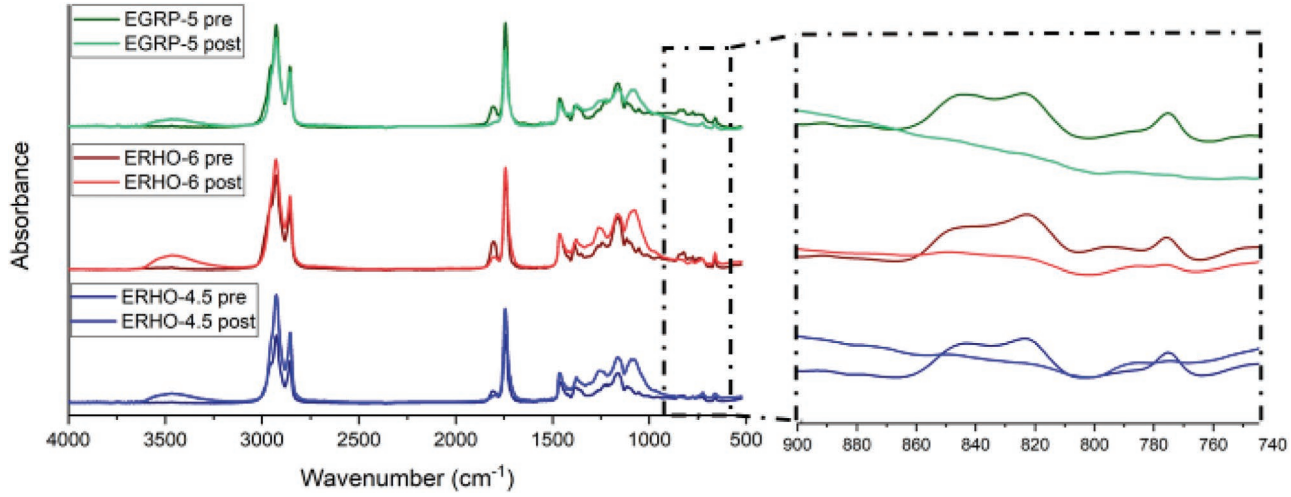

Figure 3. FTIR spectra recorded before and after the irradiation.

Table 3. Properties of the crosslinked films.

EVOs	FTIR conversion [%]	Gel content [%]	T_g_DMTA [°C]	E' at glassy state [MPa]	E' at rubbery plateau [MPa]	Crosslinking density [mmol cm^{-3}]	T_g_DSC [°C]	$T_{5\%}$ [°C]	T_{peak} [°C]	Char residue [%]
ERHO-4.5	95	94	9	47	0.3	0.03	−10	304	400	6
EGRP-5	99	98	16	653	1	0.38	−5	340	399	7
ERHO-6	93	95	57	1191	23	5.38	23	333	400	8

2854 cm^{-1} represent the $-CH_2-$ methylene asymmetrical and symmetrical stretching vibration respectively. The peak at 1745 cm^{-1} can be attributed to the −C = O ester stretching vibration. The peaks at 1465 and 1378 cm^{-1} represent the −C−H (CH_2, CH_3) scissoring and −C−H (CH_2) rocking vibration respectively. The peaks at 1162 and 1116 cm^{-1} correspond to the −C−O bending and −C−O stretching vibrations. The double peak at 840 cm^{-1} can be attributed to the C−O−C of the epoxy ring.[44]

The success of the epoxy ring opening reaction was confirmed by the disappearance of the double peaks centered at 840 cm^{-1} upon irradiation and by the appearance of two peaks, one centered at 1090 cm^{-1} and the other broad centered at 3465 cm^{-1} which can be attributed to the C−O−C ether stretching vibration and to the −OH hydroxyl group stretching vibration respectively.

The average percentages of conversion were calculated following the decrease of the double peaks centered at 840 cm^{-1}. All the data are reported in the **Table 3**.

All the UV-cured films were fully crosslinked and tack-free with a gel content always above 94% (see Table 3).

3.3. Thermal and Viscoelastic Properties

The dynamic mechanical thermal analysis (DMTA) was performed on the UV-cured films in order to fully characterize their thermal and viscoelastic properties. In fact, thanks to this technique it was possible to evaluate the storage (E') and dissipative (E'') modulus of the material in a large temperature range. The ratio of these two moduli E''/E' provides the parameter called Tanδ. The maximums of Tanδ correspond to the T_g of the materials. The tanδ curves of the UV-cured films are reported in **Figure 4**a. It is possible to observe an increase of T_g, with a shift of the maximum of tanδ curves toward higher temperature, by increasing the epoxy content of the photocurable oil, ranging from 9 to 57 °C (see data collected in Table 3). Furthermore, the Tanδ curve of ERHO-6 is broader and flatter than the others, suggesting a more heterogenous network with a larger distribution of chain relaxation.[45]

The moduli value in the rubbery plateau can be associated with the cross-linking density (ν_c) of the networks, higher the moduli value the higher the ν_c.[46] In particular, the statistical theory of rubbery elasticity was used to evaluate the cross-linking density. The ν_c ranges from 0.03 mmol cm^{-3} of ERHO-4.5 to 5.38 mmol cm^{-3} of ERHO-6. This result was expected since by increasing the epoxy content it is possible to reach a higher crosslinking density during curing. DSC analysis confirmed the same trend of T_g measured by DMTA analysis for the UV-cured films (Table 3). The Tg values obtained by DSC are lower than those obtained by DMTA; this is a very well-known behavior which can be attributed to the frequency effect.[47]

TGA analysis highlights that all the UV-cured films have high thermal stability (see Figure 4b). The $T_{5\%}$ ranges from 304 °C to 340 °C which are close to the one obtained with petroleum-based epoxy resin such as DGEBA,[19] moreover, all the crosslinked networks exhibit similar low char residue.

3.4. Surface Properties

The UV-cured films showed high solvent resistance, good surface hardness, and adhesion to the metallic substrate. The solvent resistance was measured by MEK-resistance test. Samples having higher cross-linking density showed an increase in MEK resistance, corresponding to an improvement in the chemical resistance of the coating surface (**Table 4**). The linear correlation between ν_c and the final properties of the coatings are also evident looking at the results of the scratch and pencil

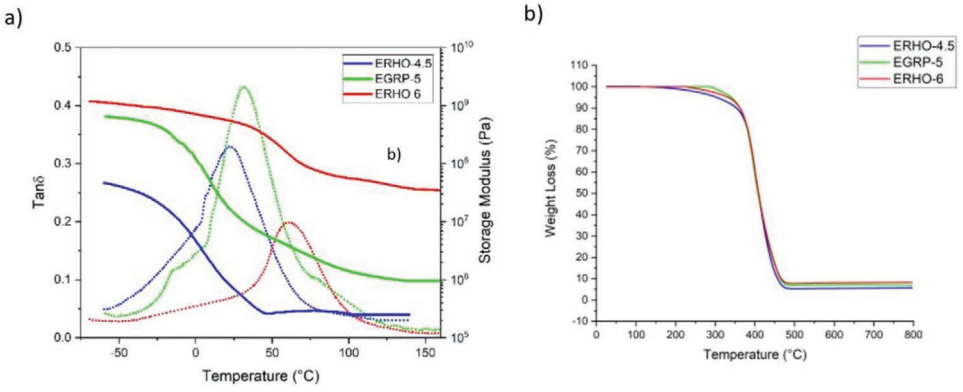

Figure 4. a) Tanδ curve and storage modulus from DMTA analysis; b) TGA analysis.

Table 4. Surface properties of the obtained coatings.

EVOs	Solvent resistance	Film hardness	Adhesion test On metal [%]	Water contact angle [°]	Diiodomethane Contact angle [°]	Surface tension [mN m^{-1}]
ERHO-4.5	50	3B	92	75.4 ± 2	38.4 ± 5	41.7
EGRP-5	100	F	93	74.9 ± 2	36.9 ± 3	42.4
ERHO-6	>200	F	96	80.7 ± 3	37.1 ± 2	41.4

hardness tests (see data Table 4), with an increase of hardness from 3B for the UV-cured ERHO-4.5 up to F for the UV-cured film ERHO-6. The percentage of adhesion, as well, increased from 92% for ERHO-4.5 to 96% for ERHO-6. All the data are reported in the Table 4.

The water contact angle values range from 75° to 81° which are slightly higher than the one obtained with UV-Cured petroleum-based resins such as 3,4-epoxycyclohexylmethyl-3,4-epoxycyclohexane carboxylate (70°).[48] This can be attributed to the presence in the monomer structure of long hydrophobic aliphatic chains. The diiodomethane contact angle was also measured in order to evaluate the surface tension of the coatings by using WORK method. All the networks possess a very similar surface energy of about 42 mN m^{-1}, close to values obtained for fossil-fuel based epoxy resin (≈40 mN m^{-1}).[49]

3.5. Anticorrosion Performance

3.5.1. Potentiodynamic Polarization

Corrosion protection effectiveness of the different formulations was assessed by means of electrochemical measurements. Potentiodynamic polarization curves were acquired for the three coatings and compared to an uncoated steel sample (bare steel). The result is shown in **Figure 5**, where one representative measurement is reported for each coating formulation. As it is possible to observe, all coatings are able to provide a good protection for the substrate, decreasing the measured current both in the cathodic and anodic part of the curve of at least two orders of magnitude. The best performance is provided by the ERHO-6 samples, which are also the only ones that do not show evidence of pitting for the whole scanned anodic overpotential. Looking at the results from the Tafel extrapolation (see **Table 5**), it is possible to note that they exhibit the highest E_{corr} values and the lowest I_{corr}, confirming their stability during the test. As a further consequence, polarization resistance is high and corrosion rate has the lowest value between the investigated coatings. ERHO-4.5 and EGRP-5 show a different behavior, characterized by higher I_{corr} values (about two orders of magnitude higher than ERHO-6) and the presence of different peaks in the anodic part of the curve. This last feature can be attributed to local breakdowns of the coating and thus to pitting phenomena. Corrosion rate values are higher for these coatings if compared to ERHO-6 samples, but still provide an effective protection to the metal substrate as can be seen looking at the values for the uncoated samples.

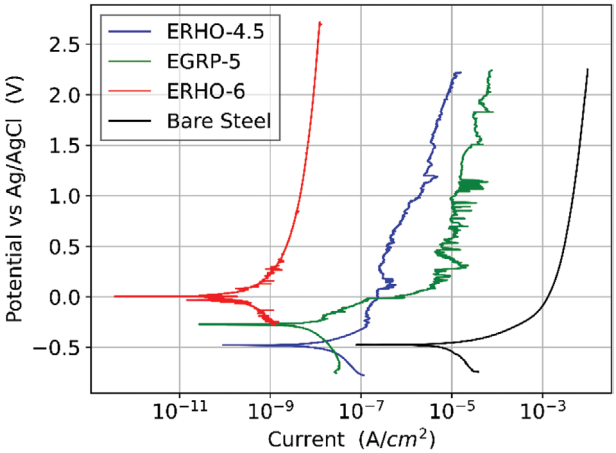

Figure 5. Potentiodynamic polarization curves for different samples measured in 0.1 M NaCl solution.

It is difficult to directly compare these results to those present in literature, mainly because many test conditions can vary, leading to different values for the investigated parameters. For example, chlorides concentration in the solution and coating thickness have a large variability in corrosion studies present in literature. Nevertheless, it is possible to assert that these formulations exhibit an effective corrosion protection behavior in an environment containing chlorides. Moreover, values of different parameters derived from potentiodymanic polarization measurements are comparable (particularly in the case of ERHO-6 samples) to those reported for epoxy resins produced from non-renewable sources.[50–52]

3.5.2. Electrochemical Impedance Spectroscopy Measurements

Further investigations on the corrosion protection behavior of these coatings have been performed by means of EIS. Actually, using this technique it is possible to assess the stability of a coating when immersed in an electrolyte solution as a function of the immersion time, studying phenomena like water absorption and coating failure. Unlike potenziodynamic polarization, EIS is non-destructive, so the measurements do not

Table 5. Results from Tafel extrapolation obtained from potentiodynamic polarization curves.

EVOs	E_{corr} [mV]	I_{corr} [A cm^{-2}]	R_p [Ohm]	Corrosion rate [mm y^{-1}]
ERHO-4.5	−290	1.06 10^{-8}	2.68 10^{7}	1.23 10^{-4}
EGRP-5	−328	1.62 10^{-8}	7.02 10^{6}	1.88 10^{-4}
ERHO-6	−57	1.67 10^{-10}	2.13 10^{8}	1.94 10^{-6}
Bare steel	−472	5.41 10^{-6}	1.28 10^{3}	6.28 10^{-2}

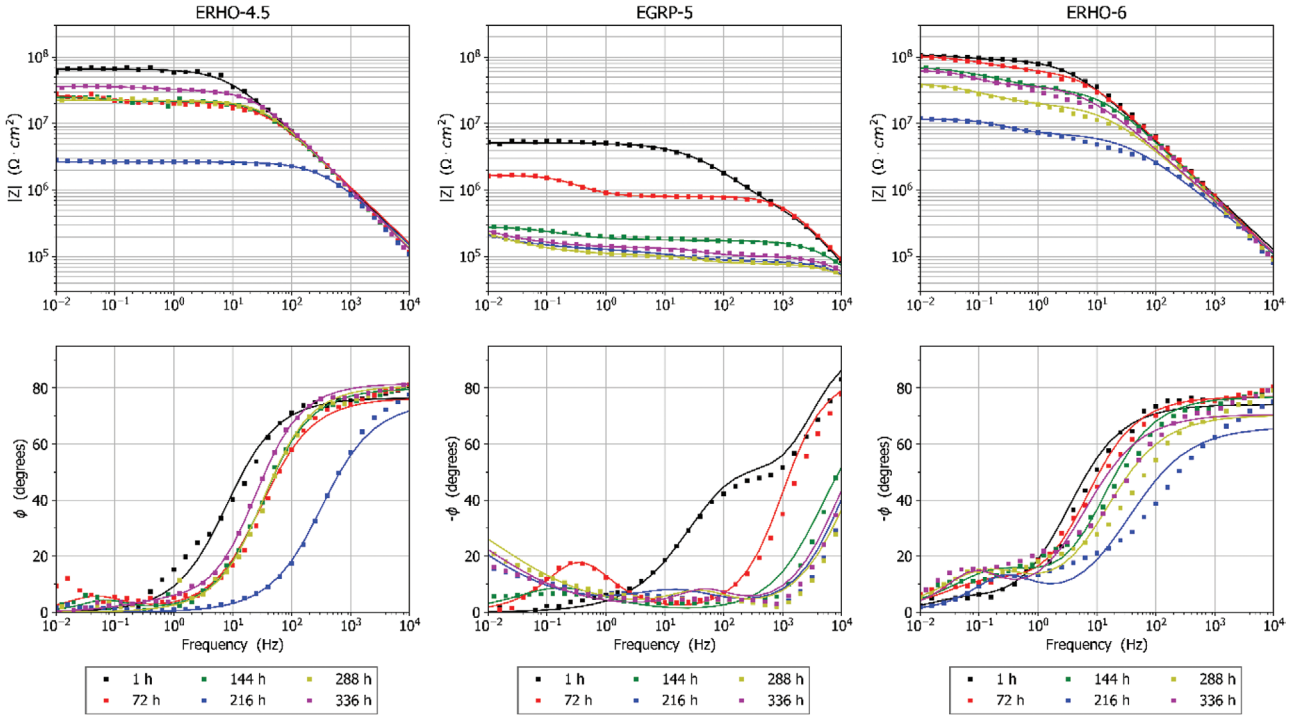

Figure 6. Impedance spectra, presented as Bode diagrams, acquired for the three coatings as a function of the immersion time in the 0.1 M NaCl solution. Dots represent the experimental points, while colored lines represent the results from the equivalent electrical circuits modelling.

damage the sample and it is thus possible to characterize the evolution of the system over time taking multiple measurements on the same sample.[53] Results are presented in **Figure 6** as Bode diagrams. It is possible to see that at the beginning of the test, that is, after 1 h of immersion in the solution, all coatings exhibit a good protective behavior. At high frequencies, a capacitive behavior can be observed, as testified by phase values close to 90°; it then changes and becomes resistive for all coatings at low frequencies, where the impedance modulus $|Z|$ reaches a plateau. The highest values for impedance modulus, which are correlated to good protective properties, are found for ERHO-4.5 and ERHO-6 samples, that reach values in the order of about 10^8 Ohm cm^2. Lower values are instead measured for EGRP-5 samples, as the impedance modulus remains below 10^7 Ohm cm^2 since the beginning of the test. Impedance moduli measured after 1 h of immersion for the different samples are close to the polarization resistance values computed by means of Tafel extrapolation (see Table 5), demonstrating a good agreement between the different techniques employed.[54]

Increasing the immersion time, different behaviors are further highlighted. EGRP-5 samples exhibit an important decrease in the modulus of impedance already after 72 h and then it stabilizes slightly above 10^5 Ohm cm^2 until the end of the test. As general rule of thumb, it is possible to state that a coating is no more protective for the metal substrate if the impedance modulus reaches values below 10^6 Ohm cm^2.[37] The loss of protective effectiveness is also testified by the decrease of the phase values below 50° for the whole frequency range. A different behavior was observed for the ERHO-4.5 and ERHO-6 samples. In this case, impedance modulus at low frequencies has a gradual decrease with immersion time (slower and less evident for ERHO-6), but then it increases again, stabilizing close to the initial values. This behavior can be attributed to the diffusion of water molecules and aggressive ions from the solution to the coating. When they reach the metal surface, this phenomenon can lead to the oxidation of the metal and thus a subsequent increase in the impedance modulus due to the localized formation of corrosion products. It is important to notice that during the whole test the impedance modulus at low frequencies remains above 10^6 Ohm cm^2 for both samples (about 10^7 Ohm cm^2 for the ERHO-6 samples); moreover, phase values at high frequencies are close to 90°, demonstrating a capacitive behavior in this part of the spectrum.

3.5.3. Modeling of Electrochemical Impedance Spectroscopy Spectra

In order to deeper analyze the results from impedance spectroscopy measurements, equivalent electrical circuit modeling was used. Impedance data were modelled using the circuit presented in Figure 5a, in order to correctly fit the two time constants present in the spectra. In order to model also the diffusion processes occurring in the second part of the test in EGRP-5 samples, these spectra were fitted using the electrical circuit shown in Figure 5b, where a Warburg impedance is in series to the resistance to charge transfer. The complete list of parameters computed by means of equivalent electrical circuit modelling can be found in Table S1, Supporting Information,

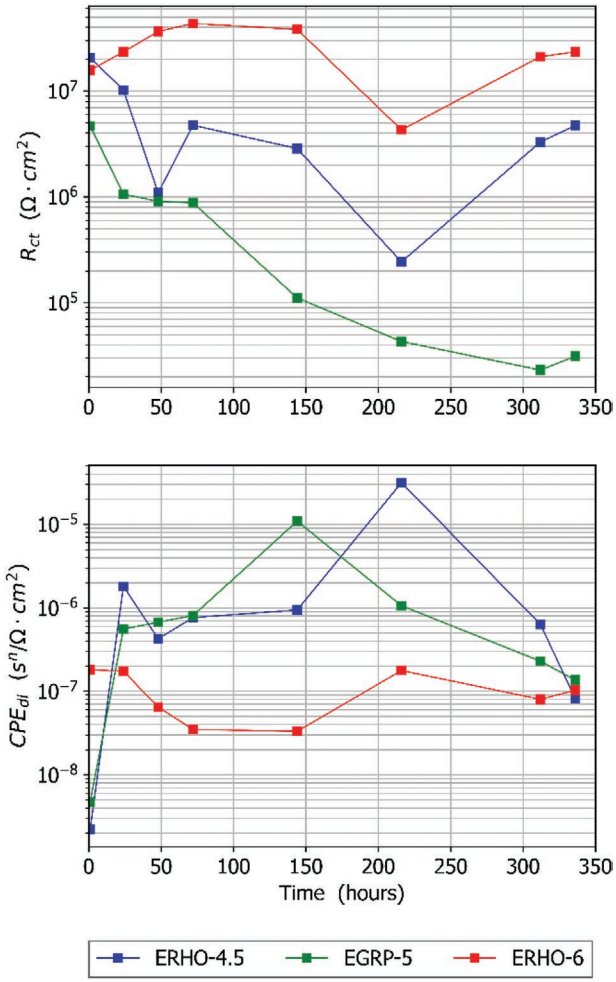

Figure 7. Trend of R_{ct} and CPE_{dl} during the corrosion test for the samples ERGO-4.5, EGRP-5, and ERHO-6.

(Additional Material), while the trend of R_{ct} and CPE_{dl} is reported in **Figure 7**. Actually, these two quantities model the interface between the coating and the metal substrate and thus their trend is generally considered the most important to study the corrosion phenomena. Focusing on the resistance to charge transfer values, it is possible to see that they remain stable for the whole duration of the test for ERHO-6 sample. There is a decrease of about one order of magnitude in the measurement acquired after 216 h but then it increases again, demonstrating the low corrosion rate for this material during the test. As far as ERHO-4.5 sample is concerned, it is possible to see that a similar trend is present, even if values are lower than those found for the ERHO-6. Then, as previously observed commenting the Bode diagrams, R_{ct} values for EGRP-5 sample have a decreasing trend that leads to the loss of two orders of magnitudes for this parameter, showing the limited performance of this coating formulation. In the second part of the test (after 216 h of immersion) the Warburg element is able to model the diffusion phenomena (see Table S1, Supporting Information), which can be identified in the impedance spectra in Figure 6 as the increase of impedance modulus and phase in the low-frequency region, where instead the other samples where characterized by a plateau.

As far as capacitance of the double layer is concerned, here modelled as a CPE, it is possible to see that for all samples it has an increasing trend, associated to the water uptake and diffusion toward the interface between the coating and the metal surface. Also in this case, the most stable behavior was found for the ERHO-6 sample. ERHO-4.5 and EGRP-5 samples are instead characterized by a sharp increase in the first 24 h of test and then stabilize to similar values. The n parameter is close to unity for all samples and this denotes a behavior for the CPE similar to an ideal capacitor.

3.5.4. Morphological Characterization

At the end of the 2-week tests, samples surface was characterized by means of electron microscopy in order to assess their morphology and detect possible defects formed during immersion in the electrolyte solution. As can be seen in **Figure 8**, ERHO-4.5 samples show the presence of some localized defects distributed on the coating surface. Analyzing these points at higher magnification, they can be identified as corrosion products formed in correspondence of localized irregularities in the coating and thus preferential paths for electrolyte diffusion through the coating toward the metal surface. They formed presumably during the central part of the immersion test, when the EIS measurements detected a decrease in the impedance modulus.

As expected, EGRP-5 samples exhibit a different morphology, in which extensive signs of corrosion are visible. The presence of irregularities on the surface (presumably due to water absorption) and corrosion products is widespread all over the area exposed to the electrolyte. Actually, for these samples EIS measurements indicated the loss of protection effectiveness, here confirmed by morphological characterization. Finally, taking into consideration ERHO-6 samples it is possible to state that no significative signs of polymer deterioration are visible and no corrosion products could be found on the sample surface. This condition was further confirmed at higher magnification. This is in agreement with electrochemical measurements, which demonstrated the good protective properties of ERHO-6 against corrosion, also after 2 weeks of immersion in the solution containing chlorides.

Even if all the EVOs precursors have similar structure and the crosslinked films showed very close water contact angle, the UV-cured films showed a wide range of thermo-mechanical properties and corrosion protection behaviors. Considering the thermo-mechanical characterization of the photocrosslinked coatings, it is possible to correlate their electrochemical behavior to their chemical-physical properties.

The enhanced corrosion protection of the ERHO-6 coatings can be ascribed to both its higher T_g and crosslinking density. It was previously demonstrated that networks with increased T_g and ν_e showed reduced swelling and lower water permeability.[55] Moreover, since all the corrosion tests were performed at room temperature (T = 20 °C), the ERHO-6 is the only coating evaluated in its glassy state. This fact means that the chain mobility within the polymer matrix is obstructed,

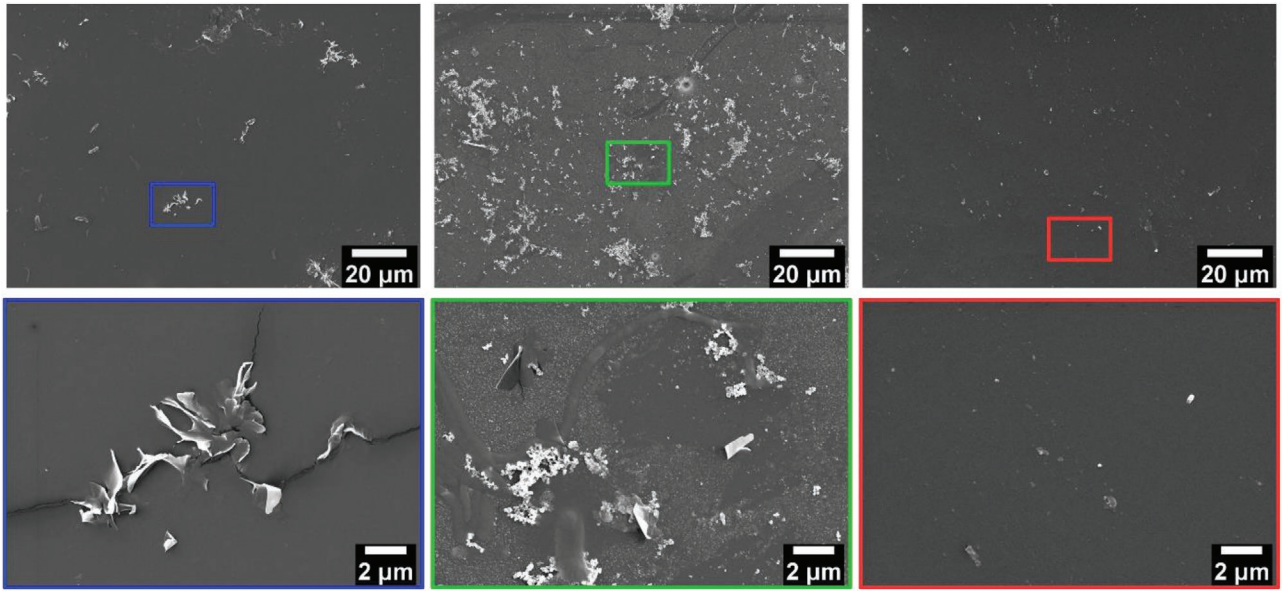

Figure 8. SEM micrographs showing surface morphology of the three coatings (from left to right: ERHO-4.5, EGRP-5, and ERHO-6) after immersion for 336 h in the 0.1 M NaCl solution. Images at the bottom are magnifications of some details.

and the thermoset behaves like a solid. The high ERHO-6 network rigidity can more effectively hinder the diffusion of water molecules and other species within the coating, resulting in an improved barrier effect against the corrosive medium.

4. Conclusions

This study provides insight into the field of the photocurable bio-based coatings. The cationic UV-curing efficiently gives rise to cross-linked networks with a high degree of conversion, a wide range of thermo-mechanical properties, and good thermal stabilities. Although the coatings have similar water contact angle and adhesion, they show different anti-corrosion behavior. The ERHO-6 coating showed the best performances with higher solvent resistance, hardness, and corrosion resistance. Its enhanced coating toughness can explain these improved performances due to high cross-linking density and T_g. Combining those factors, the coating may delay water molecules diffusion and other species through the coating, resulting in an improved barrier effect against the corrosive medium.

Our study offers a full understanding of the potentiality of applying vegetable oil as a starting monomer to produce coatings with anti-corrosion properties.

Supporting Information

Supporting Information is available from the Wiley Online Library or from the author.

Acknowledgements

The authors would like to thank Alessio Gullino for the help in FESEM analysis.

Conflict of Interest

The authors declare no conflict of interest.

Author Contributions

C.N. wrote the manuscript together with L.I. and she performed the chemico–physical characterizations of the coatings. L.I. specifically contributed to the discussion of the electrochemical results and to the modelling of the EIS spectra. S.M. and A.G., synthetized and provided the monomers. M.S. and S.G. gave suggestions on the structure of the manuscript and on the design of the experiments. All authors reviewed the manuscript.

Data Availability Statement

Research data are not shared.

Keywords

bio-based resins, cationic UV-curing, coatings, corrosion resistance

Received: January 11, 2021
Revised: March 2, 2021
Published online: March 19, 2021

[1] R. Auvergne, S. Caillol, G. David, B. Boutevin, J. P. Pascault, *Chem. Rev.* **2014**, *114*, 1082.
[2] F. Deflorian, L. Fedrizzi, S. Rossi, P. L. Bonora, *Electrochim. Acta* **1999**, *44*, 4243.
[3] D. Zhang, H. Qian, L. Wang, X. Li, *Corros. Sci.* **2016**, *103*, 230.
[4] X. M. Li, D. Reinhoudt, M. Crego-Calama, *Chem. Soc. Rev.* **2007**, *36*, 1350.

[5] J. Zhang, W. Zhang, L. Wei, L. Pu, J. Liu, H. Liu, Y. Li, J. Fan, T. Ding, Z. Guo, *Macromol. Mater. Eng.* **2019**, *304*, 1900374.
[6] Y. Li, H. Yang, F. Wang, Y. Huang, *J. Appl. Polym. Sci.* **2021**, *138*, 49866.
[7] S. Zhenga, D. A. Bellido-Aguilara, Y. Huanga, *Surf. Coat. Technol.* **2019**, *363*, 43.
[8] S. Ma, T. Li, X. Liu, J. Zhu, *Polym. Int.* **2016**, *65*, 164.
[9] S. Zhao, M. M. Abu-Omar, *ACS Sustainable Chem. Eng.* **2017**, *5*, 5059.
[10] J. Xin, P. Zhang, K. Huang, J. Zhang, *RSC Adv.* **2014**, *4*, 8525.
[11] J. Qin, H. Liu, P. Zhang, M. Wolcott, J. Zhang, *Polym. Int.* **2014**, *63*, 760.
[12] M. Fache, E. Darroman, V. Besse, R. Auvergne, S. Caillol, B. Boutevin, *Green Chem.* **2014**, *16*, 1987.
[13] E. Desnoes, L. Toubal, A. H. Bouazza, D. Montplaisir, *Polym. Eng. Sci.* **2020**, *60*, 2593.
[14] A. S. Amarasekara, R. Garcia-Obergon, A. K. Thompson, *J. Appl. Polym. Sci.* **2019**, *136*, 47000.
[15] M. Kathalewar, A. Sabnis, *J. Coat. Technol. Res.* **2014**, *11*, 601.
[16] M. Sangermano, N. Razza, J. V. Crivello, *Macromol. Mater. Eng.* **2014**, *299*, 775.
[17] S. Ma, T. Li, X. Liu, J. Zhu, *Polym. Int.* **2016**, *65*, 164.
[18] S. Kumar, S. K. Samal, S. Mohanty, S. K. Nayak, *Polym.—Plast. Technol. Eng.* **2018**, *57*, 133.
[19] F. Ng, G. Couture, C. Philippe, B. Boutevin, S. Caillol, *Molecules* **2017**, *22*, 149.
[20] J. V. Crivello, R. Narayan, *Chem. Mater.* **1992**, *4*, 692.
[21] H. J. Park, C. Y. Ryu, J. V. Crivello, *J. Polym. Sci., Part A: Polym. Chem.* **2013**, *51*, 109.
[22] F. Jaillet, E. Darroman, B. Boutevin, S. Caillol, *OCL: Oilseeds Fats, Crops Lipids* **2016**, *23*, D511.
[23] C. Noè, S. Malburet, E. Milani, A. Bouvet-Marchand, A. Graillot, M. Sangermano, *Polym. Int.* **2020**, *69*, 668.
[24] S. D. Vacche, A. Vitale, R. Bongiovanni, *Molecules* **2019**, *24*, 3858.
[25] S. Nameer, D. B. Larsen, J. O. Duus, A. E. Daugaard, M. Johansson, *ACS Sustainable Chem. Eng.* **2018**, *6*, 9442.
[26] Q.-B. Nguyen, H. Vahabi, A. R. de Anda, D.-L. Versace, V. Langlois, C. Perrot, V.-H. Nguyen, S. Naili, E. Renard, *Sustainable Chem.* **2021**, *2*, 24.
[27] C. Noè, S. Malburet, A. Bouvet-Marchand, A. Graillot, C. Loubat, M. Sangermano, *Prog. Org. Coat.* **2019**, *133*, 131.
[28] S. Malburet, D. Mauro, C. Noè, A. Mija, **2020**, *10*, 41954.
[29] W. Hasan, *J. Food Process Eng.* **2020**, *43*, e13396.
[30] Z. Yang, H. Peng, W. Wang, T. Liu, *J. Appl. Polym. Sci.* **2010**, *116*, 2658.
[31] P. J. Flory, *Polym. J.* **1985**, *17*, 1.
[32] V. G. Papadakis, *J. Appl. Polym. Sci.* **1969**, *13*, 1741.
[33] L. Iannucci, M. Parvis, E. Di Francia, S. Grassini, *IEEE Trans. Instrum. Meas.* **2018**, *67*, 1142.
[34] A. J. Bard, L. R. Faulkner, *Electrochemical Methods: Fundamentals and Applications*, John Wiley & Sons, New York **2001**.
[35] M. Stern, A. L. Geary, *J. Electrochem. Soc.* **1957**, *104*, 56.
[36] L. E. Sebar, L. Iannucci, E. Angelini, S. Grassini, M. Parvis, *IEEE Trans. Instrum. Meas.* **2021**, *70*, 1.
[37] A. Amirudin, D. Thierry, *Prog. Org. Coat.* **1995**, *26*, 1.
[38] M. Rajabi, G. R. Rashed, D. Zaarei, *Corros. Eng., Sci. Technol.* **2015**, *50*, 509.
[39] M. E. Orazem, B. Tribollet, *Electrochemical Impedance Spectroscopy*, John Wiley & Sons, Hoboken, NJ **2017**.
[40] C. A. W. Allen, K. C. Watts, R. G. Ackman, M. J. Pegg, *Fuel* **1999**, *78*, 1319.
[41] S. Sinadinović-Fišer, M. Janković, Z. S. Petrović, *JAOCS, J. Am. Oil Chem. Soc.* **2001**, *78*, 725.
[42] L. Yang, H. Dai, A. Yi, B. Lin, G. Li, *J. Therm. Anal. Calorim.* **2008**, *93*, 875.
[43] M. Yan, E. M. Frank, E. W. Cochran, *JAOCS, J. Am. Oil Chem. Soc.* **2018**, *95*, 209.
[44] H. Yang, J. Irudayaraj, *JAOCS, J. Am. Oil Chem. Soc.* **2000**, *77*, 291.
[45] A. Cosola, R. Conti, H. Grützmacher, M. Sangermano, I. Roppolo, C. Pirri, A. Chiappone, *Macromol. Mater. Eng.* **2020**, *305*, 2000350.
[46] K. S. Anseth, C. M. Wang, C. N. Bowman, *Polymer* **1994**, *35*, 3243.
[47] L. E. Nielsen, R. F. Landel, *Mechanical Properties of Polymers and Composites*, CRC Press, Boca Raton, FL, USA **1993**.
[48] M. Sangermano, A. Perrot, A. Gigot, P. Rivolo, F. Pirri, *Macromol. Mater. Eng.* **2016**, *301*, 93.
[49] F. Awaja, M. Gilbert, G. Kelly, B. Fox, P. J. Pigram, *Prog. Polym. Sci.* **2009**, *34*, 948.
[50] M. Rajabi, G. R. Rashed, D. Zaarei, *Corros. Eng., Sci. Technol.* **2015**, *50*, 509.
[51] S. Pourhashema, M. R. Vaezia, A. Rashidib, M. R. Bagherzadeh, *Corros. Sci.* **2017**, *115*, 78.
[52] Y.-T. Lin, T.-M. Don, C.-J. Wong, F.-C. Meng, Y.-J. Lin, S.-Y. Lee, C.-F. Lee, W.-Y. Chiu, *Surf. Coat. Technol.* **2019**, *374*, 1128.
[53] L. Iannucci, J. F. Ríos-Rojas, E. Angelini, M. Parvis, S. Grassini, *Eur. Phys. J. Plus* **2018**, *133*, 522.
[54] A. Nishikata, Y. Ichihara, T. Tsuru, *Corros. Sci.* **1995**, *37*, 897.
[55] G. Teng, M. D. Soucek, *Macromol. Mater. Eng.* **2003**, *288*, 844.